

AN ELASTO/PLASTIC MODEL OF THE ULTRASONIC ADDITIVE MANUFACTURING

Q. Mao, N. Coutris, and G.M. Fadel

Department of Mechanical Engineering, Clemson University, SC 29630

Abstract

Ultrasonic additive manufacturing (UAM) is a solid-state fabrication process that utilizes ultrasonic energy to bond metal foils layer by layer. It has been shown that bond formation is closely related to the plastic deformation of the material at the bonding interface. As a result, a material model is necessary to characterize the elastic and plastic deformation of material under UAM conditions. The existing material models for UAM suffer from the following issues: 1) the models are established based on experimental data of a material different from the material used in UAM. 2) The models have not fully accounted for the influential factors in UAM. Therefore, a new material model is established by modifying the Johnson-Cook model which is known to be simple but effective to capture plasticity at elevated temperature and high strain rate. The model is based on experiments carried out on aluminum 6061-T6 which has been extensively used in the ultrasonic additive manufacturing. Ultrasound-induced effects including strain hardening, strain rate hardening, acoustic softening, and thermal softening are considered in the model. In addition to plasticity, the bond formation/plastic deformation is also profoundly affected by the dynamics of the built feature which has not been considered in combination with plasticity in the existing studies. As a result, a UAM model is established in which both the mechanical and dynamic effects are taken into account. The model is shown to characterize well the plastic deformation at the bonding interface both qualitatively and quantitatively by comparing its predictions with experimental observations.

Introduction

Although the UAM has only existed for a decade [1], its bonding process stems from the ultrasonic metal welding (UMW) which was invented over 50 years ago and is extensively implemented in industry. Numerous experimental investigations have been conducted to understand the bond mechanism of UMW [2-6]. However, the mechanics behind the bonding process are still far from being completely understood. Particularly, the plastic shear deformation of materials at the bonding interface, which has been highlighted as a critical factor for bond formation [5], lacks full investigation and characterization. In addition, the dynamics of the built feature also have an influence on bond formation: the built feature undergoes resonance at a critical aspect ratio and reduces the differential motion between the top foil and the built feature. The loss of differential motion leads to loss of sufficient friction and thus results in bonding failure. Thus, the goals of this paper include: 1) characterizing the material behavior under UAM conditions and establishing a generic material model that is capable to predict the bonding mechanics. 2) Studying the influence of the change of macroscopic dynamics of the system on the bonding mechanics. 3) Relating bond mechanics to bond quality.

Motivation

The understanding of fundamental mechanisms of UAM bonding is limited. While it has been agreed by researchers that in general the bond formation undergoes three stages: 1) plastic deformation of asperities and break-up of surface oxides, 2) increasing contact area of pure metals with plastic flow enclosing the voids, and 3) bond formation and the maintaining of bonds through plastic deformation, yet the mechanisms behind bond formation is still arguable and even contradictory [2-5]. Early studies by Joshi showed that bonds are formed as the material undergoes diffusion, localized melting, and mechanical interlocking [7]. In support of Joshi, Gunduz et al. observed significant plastic flow at a strain rate of up to 10^3 /s. The plastic flow on one hand initiates diffusion by increasing vacancy concentration, on the other induces localized melting through adiabatic heating [6]. Lee et al. observed mechanical interlocking between soft and hard material while bonding Cu to Ni-plated Cu [4]. Severe plastic deformation in copper is observed. According to Janaki Ram, however, the bonding process is universally due to solid-state metallic adhesion which involves adhesion of layers of atoms that create an apparent interfacial bond strength across the interface [3][8]. They further pointed out that the plastic deformation played a major role in all the three stages of bond formation as they repeat themselves in welding process. Recrystallization is reported by several researchers [4] [9] [10]. Recrystallization is observed to be localized at the bond interface and is caused by heat generated from plastic deformation and interfacial friction. While the actual mechanism of UMW is arguable and could be material specific, it is evident that plastic deformation serves as a key component in bond formation. Without sufficient plastic deformation the bond would be degraded or even fail. If the plastic deformation at the bond interface can be quantified, it is possible to use it as an indicator for predicting bond quality and thus connecting UAM operating parameters (vibration amplitude, compression load, and weld speed) to bond quality through computation. In order to quantify the plastic deformation, the bonding mechanics of UAM should be understood and a model be established.

Pioneering work is done by de Vries who studied the mechanics of UMW, which shares a similar bonding principle with UAM but generates bonds only at contact points rather than along contact lines. They studied the internal stress within the top and bottom foil as well as frictional stress at the bond interface, and established a bond criterion that requires the internal stress to be greater than the yield strength of the material to initiate bonding. The internal stress is calculated based on both the yield stress which depends solely on temperature, and the compressional stress. Behind this mechanics model, several assumptions are made: 1) the plasticity is assumed to be perfect (free of hardening) and yield stress decreases as local temperature increases. 2) The friction coefficient at the bonding interface is assumed as a constant. 3) The ultrasonic sonotrode has a flat surface and thus the stress state is 2-D. While the mechanics model and the associated bond criterion provides insights to the understanding of UMW bonding, it is far from enough to characterize the mechanics in UAM. First, the yield stress under UAM condition is affected by multiple factors: plastic strain, high plastic strain rate, ultrasonic energy, and thermal energy. Second, the two mating foils undergo stick-slip friction which is affected by the dynamics of the built feature [11]. The friction coefficient is not constant but rather temperature-dependent [12]. Third, the stress state in UAM is not 2-D plane stress since the sonotrode is of cylindrical shape rather than flat. Therefore the 3-D stress state has to be considered in the mechanics model.

Another factor that prevents the UMW model from being implemented for UAM is the difference in the dimensions of foils. While the dimension of the foils for UMW is flexible, the foils used for UAM process have fixed dimensions: 0.94 in. (23.88 mm) in width, 0.0059 in. (0.15 mm) in thickness, and customized length within the work space of UAM. Due to the small foil thickness, the dynamics of the top foil is generally insignificant when compared with that of the built feature and therefore the force required to excite the top foil is neglected.

UAM models were also established to understand the UAM bonding mechanics [13-15]. In these models, the plasticity of the material models are of critical importance. Siddiq and Ghassemieh modified the cyclic plasticity model proposed by Lemaitre and Chaboche to account for the acoustic and thermal softening effects [13] [16]. The cyclic plasticity model, however, is based on cyclic loading tests that are carried out at a strain rate ($10^{-3}/s$) much lower than that of UAM ($10^3 \sim 10^4/s$), and on a material different from what has been used for UAM. As a result, the hardening effects due to strain rate are not taken into account. Additionally, the experimental data used for characterization of acoustic softening effect is from aluminum single crystal which is much softer than the aluminum alloy used in UAM. Kelly et al. utilized a power law function to characterize the stress-strain relationship in the plastic region for a UAM model bonding aluminum alloy 1100 [14]. In the stress-strain relationship, the thermal softening effect is characterized by the exponential term and the acoustic softening by adding a factor to the power law function. Due to the lack of experimental investigation, the power law plasticity model is built on data of aluminum single crystal. The effect of strain rate is not considered. Siddiq and El Sayed modified a crystal plasticity model to account for acoustic and thermal softening in UAM [15]. The model parameters are optimized to fit the stress strain curves of aluminum single crystal. The model is then extended to polycrystalline aluminum based on EBSD studies of aluminum 6061-O. In this way, they try to understand the mechanism of acoustic and thermal softening in UAM at a microscopic scale. Although the crystal plasticity model reflects the change in microstructure of the material, the number of model parameters significantly exceeds the number of observable parameters due to the complexity of the model and the lack of experimental investigation, and an optimization tool has to be introduced, which undermines the reliability of the model. In summary, the existing UAM plasticity models suffer from the following issues: 1) models are built on experimental data from a different test condition or a different material, 2) models are too simple to fully characterize or too complicated to realistically reflect the material behavior. As a result, an appropriate material model should be established such that it can fully capture the material behavior by accounting for all the influential factors and its model parameters are sufficiently calibrated by experimental data of the correct material.

While the plasticity governs the plastic stress in response to strain, the dynamics of the built feature also have a fundamental influence on the plastic stress through friction. As additional layers are deposited, the differential motion between the sonotrode and the built feature changes, which affects the interfacial frictional forces and thus the plastic shear deformation at the interface. Robinson et al. first documented the increasing deflection as the height of the built feature approaches its width (i.e. height-to-width ratio equals 1) and attributed the phenomenon to a lack of stiffness of the built feature with respect to the vibrating sonotrode [18]. Alternatively, Zhang and Li associated the increase of deflection to a dynamic effect of the superposition of traveling waves imposed by the vibrating sonotrode [12]. Gibert et al. found that beyond the critical height-to-width ratio, bonding can be reinitiated and therefore the loss of stiffness is a dynamic effect

[11]. Furthermore, by studying the dynamics of the built feature they show that the built feature is close to resonance at the as height-to-width ratio approaches 1 under excitation of the ultrasonic sonotrode. As a result, the vibration of the built feature is synchronized with that of the sonotrode resulting in lack of differential motion for initiating frictional force and plastic shear force. This change of dynamics has not been accounted in the studies of bonding mechanics and therefore its effect on bond formation is not clear.

The Material Model

The material under study is aluminum 6061, which is selected for its extensive implementation in UAM as well as the availability of data under a variety mechanical tests and studies. For the experimental investigation, aluminum 6061-T6 are purchased from McMaster Carr and machined to the shape of tensile specimens. The material composition of aluminum 6061 is shown in table 1 (provided by manufacturer).

Table 1 Material composition of aluminum 6061-T6

Composition	Weight %
Aluminum	95.1-98.2
Silicon	0.4-0.8
Iron	0-0.7
Copper	0.05-0.4
Manganese	0-0.15
Magnesium	0.8-1.2
Chromium	0.4-0.8
Nickel	0-0.05
Zinc	0-0.25
Titanium	0-0.15
Zirconium	0-0.25
Other	0.15

In this material model, Hooke's Law is defined in the pure elastic region whereas in the plastic region, the material is assumed to be isotropic, strain hardened, strain-rate sensitive, acoustic softenable, and temperature sensitive. The total strain tensor $\underline{\varepsilon}$ can be decomposed into elastic and plastic strain tensors:

$$d\underline{\varepsilon} = d\underline{\varepsilon}_e + d\underline{\varepsilon}_p \quad (1)$$

In the elastic deformation region:

$$\underline{\sigma} = \underline{C}(\underline{\varepsilon} - \underline{\varepsilon}_p) \quad (2)$$

The von Mises yield criterion and the associated flow rule are used to determine the conditions necessary for the onset of plastic deformation and the rate of change of plastic strain components as plastic deformation proceeds. The von Mises yield criterion requires the von Mises equivalent stress to be equal to the yield strength of the material for plastic deformation to take place. The yield function (criterion) and the associated flow rule are written:

$$f(\bar{\sigma}) = |\bar{\sigma} - \alpha| - (\sigma_0 + R) = 0 \quad (3)$$

$$d\varepsilon_p = d\lambda \frac{\partial f}{\partial \bar{\sigma}} \quad (4)$$

Where $\bar{\sigma}$ is the von Mises equivalent stress, α is the back stress in kinematic hardening. Since kinematic hardening is not considered: $\alpha = 0$. σ_0 is the initial yield stress, R is the isotropic hardening term. ε_p is the plastic strain of the material, $d\lambda$ is a plastic multiplier.

In this study, the Johnson-Cook (JC) model [19] is selected and modified to characterize the material plasticity for its simple mathematical form and extensive application. Although the model is completely empirical, it is effective in characterizing deformation of large plastic strain, in high plastic strain rate, and at elevated temperature. Additionally, the JC model is a particular type of von Mises plasticity model with an explicit form of hardening law and rate dependence. The original JC model is written [19]:

$$\sigma = (A + B\bar{\varepsilon}^n)(1 + C \ln \frac{\dot{\bar{\varepsilon}}}{\dot{\bar{\varepsilon}}_0})(1 - T^{*m}) \quad (5)$$

Where $\bar{\varepsilon}^n$ is the equivalent plastic strain, $\dot{\bar{\varepsilon}}$ is the equivalent plastic strain rate, $\dot{\bar{\varepsilon}}_0$ is a reference equivalent plastic strain rate defined as: $\dot{\bar{\varepsilon}}_0 = 1/s$. A is the yield strength measured at zero-plastic-strain, unit-plastic-strain-rate, and room-temperature. B is the strain-hardening constant, n the strain-hardening exponent, C the strain-rate constant, m the thermal-softening exponent, and T^* a room-temperature (T_{room})-based dimensionless temperature defined as: $T^* = \frac{T - T_{room}}{T_{melt} - T_{room}}$, where T_{melt} is the melting temperature. The first term defines the strain hardening, the second term defines the strain rate hardening, and the third term defines the softening at elevated temperature. At room temperature ($T^* = 0$) and at the reference strain rate $\dot{\bar{\varepsilon}} = \dot{\bar{\varepsilon}}_0$, the JC model is reduced to:

$$\sigma = A + B\bar{\varepsilon}^n \quad (6)$$

A set of parameters for aluminum 6061-T6 can be obtained based on the quasi-static tensile test of aluminum 6061-T6: $A = 311.22 \text{ MPa}$, $B = 240.11 \text{ MPa}$, $n = 0.37$.

The JC model, despite its mathematical simplicity and modeling advantages, has a limitation to characterize plasticity with accuracy under the conditions in which high strain rate and ultrasound-induced softening are involved. It has been shown by multiple investigations that metals with face-centered-cubic (f.c.c.) structure demonstrate a dramatic increase of dependence of dynamic flow stress on the instantaneous strain rate as the strain rate exceeds certain threshold (typically around $10^3/s$) (fig. 1) [20][21]. It is believed that this abrupt change of strain rate sensitivity of the flow stress is due to the change of deformation mechanism. At low strain rate, the deformation is governed by the cutting or by-passing of obstacles by the dislocations. As the strain rate exceeds the threshold, the deformation starts to be controlled by phonon drag forces and the flow stress necessary to deform the material increases abruptly. This change of mechanism, however, is beyond the modeling capability of the standard JC model [20]. As a result, the JC model has to be modified such that both mechanisms are taken into account. Lesuer et al. proposed

a material model which utilizes different equations for characterizing the strain rate dependence based on the different mechanisms [20]. At low strain rate, a relation in form of Arrhenius equation is introduced based on the work of Frost and Ashby [23]:

$$\dot{\epsilon}_1 = \dot{\epsilon}_0 \exp\left[\frac{Q}{kT} \left(1 - \frac{\sigma}{\tau}\right)\right] \quad (7)$$

Where $\dot{\epsilon}_1$ represents the strain rate at which cutting and bypassing of obstacles by the dislocation is dominant, $\dot{\epsilon}_0$ is a reference strain rate, Q is the activation energy, k is Boltzmann's constant, σ is the flow stress, τ is the strength of obstacles at 0 K, and T is temperature in Kelvin. At high strain rate, the relation is a power law equation:

$$\dot{\epsilon}_2 = C_1 \sigma^{C_2} \quad (8)$$

Where $\dot{\epsilon}_2$ represents the strain rate at which the phonon drag force on dislocation is dominant, C_1 and C_2 are constants whose values are obtained through curve fitting. The relations at low and high strain rates are combined to obtain the effective strain rate:

$$\dot{\epsilon}_{eff} = \frac{\dot{\epsilon}_1 \dot{\epsilon}_2}{\dot{\epsilon}_1 + \dot{\epsilon}_2} \quad (9)$$

Similar material models can also be found in work by Sakino [21] and Manes et al.[24].

The typical UAM processes involve strain rate at $10^3 \sim 10^4$ /s. The range of the shear strain rate can be calculated with the assumptions: 1) there exists no slip between the sonotrode and the top foil, i.e. the top surface of the top foil vibrates at the same amplitude as the sonotrode, 2) the bottom surface is fully welded to the built feature and is therefore fixed (fig. 2). The vibration amplitude A varies between 5 to 50 μm while the thickness of the top foil t is roughly 150 μm . As a result, the shear strain and strain rate of the top foil can be estimated:

$$\tau = \frac{A}{t} \quad (10)$$

$$\dot{\tau} = \frac{\tau}{T/4} \quad (11)$$

The calculated shear strain rate ranges from 2.66×10^3 to $2.66 \times 10^4 \text{ s}^{-1}$. This range, however, falls around the turning point which indicates the transition of mechanisms in the rate sensitivity diagram. Since in real material, the transition of mechanism will not take place in all forest dislocations simultaneously, the sharp turn predicted by the proposed material model does not align with the experimental data.

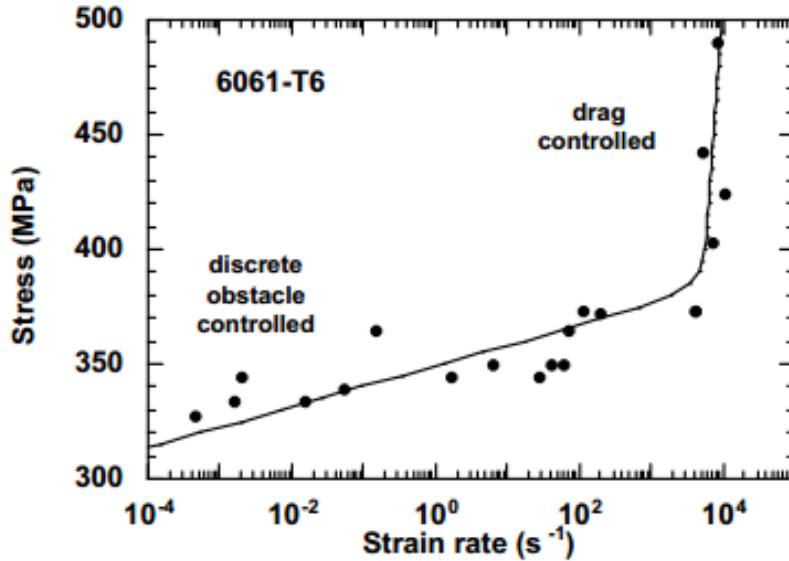


Fig.1 The strain rate sensitivity diagram of aluminum 6061-T6. Experimental data are taken from [20] and [22].

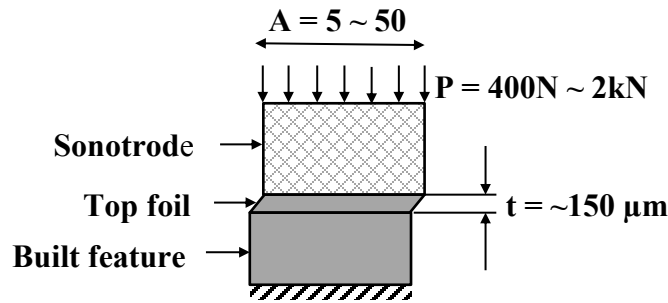


Fig.2 Schematics of the interaction between sonotrode and top foil.

In order to better characterize the flow stress at transition phase of the mechanisms, more experimental data are studied to find a model that works better specifically for the UAM. Fig. 3 shows the flow stress-strain rate diagram presented by Yadav et al. [25]. They collected experimental data of aluminum 6061-T6 from multiple studies and specifically examined the change of flow stress at the transition phase (fig. 3). Based on the data provided, a material model similar to that of Yadav et al. is implemented [25]:

$$\frac{\bar{\sigma}}{\sigma_0} = C + D \left(\frac{\dot{\epsilon}}{\dot{\epsilon}_0} \right)^b \quad (12)$$

Where σ_0 is the stress at the reference strain rate $\dot{\epsilon}_0 = 1/s$. C , D , and m are constants whose values are determined by curve fitting: $C = 0.46$, $D = 0.49$, $b = 0.10$. The comparison between the prediction of the model and the experimental data is shown in fig. 4. Based on the observation of little variation in shapes of the stress-strain curves at different strain rates, assumption has been made that the shapes of hardening curves at different strain rates are identical.

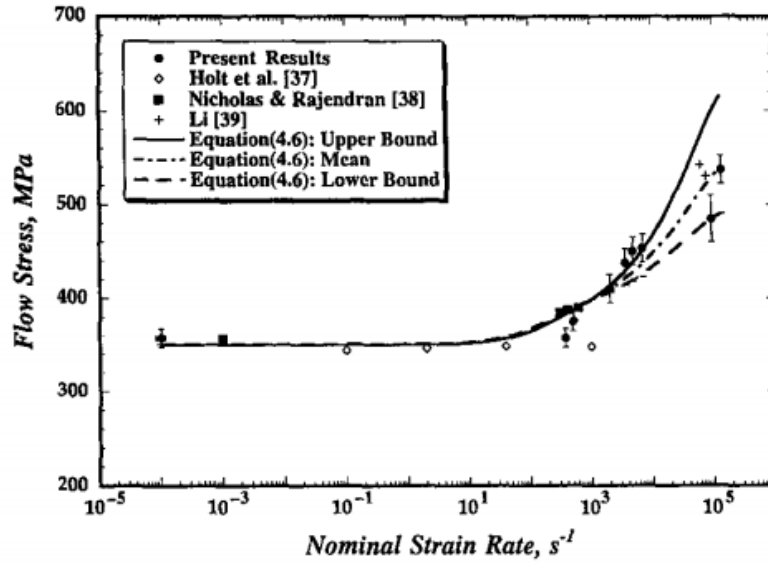


Fig. 3 Strain rate sensitivity diagram of aluminum 6061-T6.

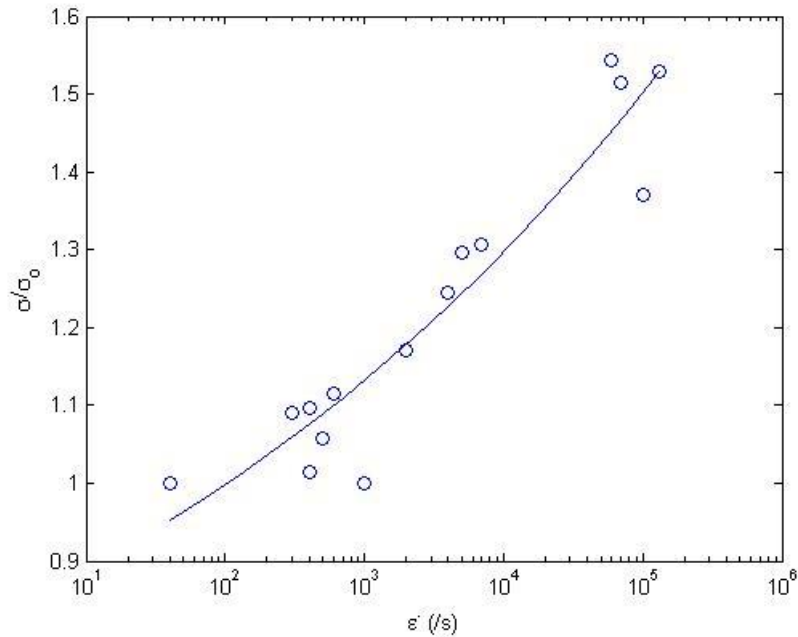


Fig. 4 Comparison of strain rate sensitivity between experimental data and model prediction at strain rate range of the UAM

In addition to strain rate sensitivity, ultrasonic energy in UAM has been shown to have a significant effect on the plastic deformation of materials known as “acoustic softening”. Early documentation of this phenomenon is done by Blaha and Lengenecker, who observed instantaneous decreases and “zero plastic stress” in aluminum single crystals and a variety of metals as ultrasonic energy is applied to a specimen in tensile tests [17]. Moreover, it is shown from the stress-strain curves that the acoustic softening is similar to softening under heating. However, the energy consumption from the ultrasonic process is much less than that from the heating process. In order to better understand and characterize the softening effects, experimental investigations are conducted for aluminum 6061-T6. The key observation is that the reduction of

the plastic stress is linearly proportional to the input of the ultrasound intensity (fig. 5). No macroscopic temperature increase is observed [26]. As a result, the JC model is modified such that the stress reduction due to ultrasound can be characterized as a linear function of the ultrasound intensity [26].

$$\frac{\bar{\sigma}}{\bar{\sigma}_0} = 1 - dI_u \quad (13)$$

Where $\bar{\sigma}$ is the flow stress under ultrasonic irradiation, and $\bar{\sigma}_0$ is the reference flow stress without ultrasonic irradiation. Both $\bar{\sigma}$ and $\bar{\sigma}_0$ are taken as averages of the stresses measured at true plastic strain $\varepsilon_p = 0.2$ and $\varepsilon_p = 0.3$ in order to obtain an accurate measuring of stress reduction. I_u is the ultrasound intensity, and d is a constant that fits the model to experimental data. At room temperature and reference strain rate, the value of d is determined as $d = 1.2 \times 10^{-4}/\text{J}$. Notice that in the experimental study of acoustic softening, the total ultrasonic energy E_u can be directly measured by the ultrasonic welder power supply [26]. In the UAM process, while the sonotrode amplitude is known, a direct measure of ultrasonic energy is not applicable. In order to estimate the applied energy, a relation is introduced to associate the ultrasound intensity to the oscillation magnitude of the ultrasonic field. The relation is written as [27]:

$$I_u = \rho \bar{A}^2 \omega^2 c \quad (14)$$

Where \bar{A} is the equivalent oscillation amplitude of the ultrasound field. ρ is the density of the medium, c is the speed of sound in the medium, and ω is the angular frequency of the ultrasound, defined as $\omega = 2\pi f$. f is the frequency of ultrasound and is fixed at 20 kHz. Since the bonding interface is very close to the sonotrode surface (roughly 0.1 mm), it is assumed that the oscillation amplitude of the ultrasonic field is the same as the amplitude of the sonotrode. Consequently, the ultrasound intensity can be characterized using vibration amplitude. By introducing equation (13) and (14), the acoustic softening can be incorporated into the stress-strain relation and thus the plasticity model (fig. 6). This characterization relies on the assumption that the amplitude of the ultrasound at the bonding interface equals the vibration amplitude of the sonotrode. In reality, however, intermittent slip takes place between the top foil and sonotrode, as well as between the top foil and the built feature which leads to an overestimation of the energy input at the bonding interface. On the other hand, the acoustic softening effect of the ultrasonic energy is underestimated in the experimental investigation due to the fact that a portion of the delivered ultrasonic energy is dissipated in the supporting structures rather than the in the specimen.

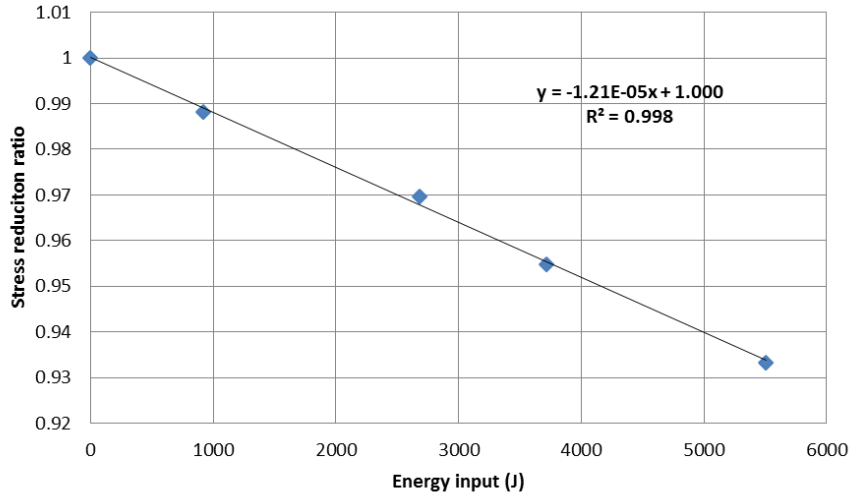


Fig. 5 The stress reduction is linearly proportional to ultrasonic energy input [26]

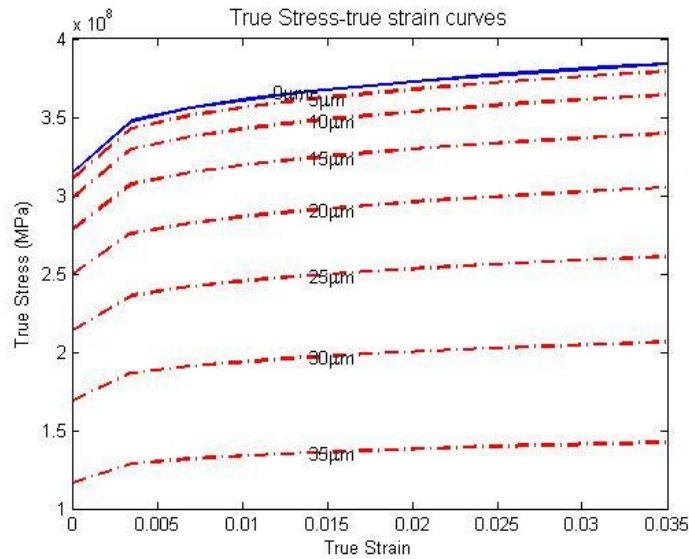


Fig. 6 The softening of aluminum 6061-T6 predicted by the model.

The temperature effects on aluminum 6061-T6 is modeled using the original JC model based on the work of Banerjee and Bhawalkar [28] who studied plasticity of the aluminum 6061-T6 at the elevated temperature and strain rate. In the UAM process, the ambient temperature is typically controlled to 300°F (around 150 °C). However, the local temperature at the bonding interface could be significantly higher due to interfacial friction and severe plastic deformation. Based on the experimental data provided, the exponential constant within the model is determined: $c = 0.68$, and the melting temperature is set to $T_m = 1000 \text{ K}$.

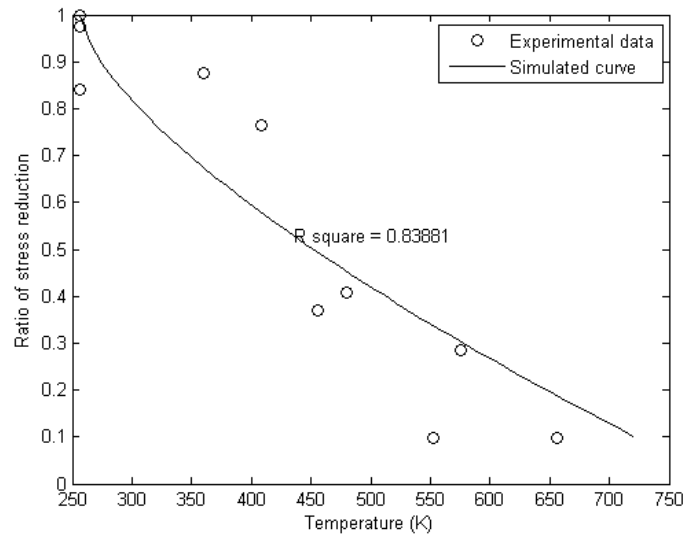


Fig.7 The comparison of experimental data and model prediction of the stress reduction due to temperature in aluminum 6061-T6.

As a result, the modified JC model is obtained by incorporating the effects of high strain rate, acoustic softening, and temperature (equation (14)). The constants are given in table 2. Furthermore, the modified JC model and the classical JC model are evaluated in terms of their performances in characterizing different material behaviors under conditions of UAM process (Table 3). In the next section, the modified JC model will be implemented to a finite element UAM model for understanding the material deformation in UAM bonding process.

$$\sigma = (1 - dI_u)(A + B\bar{\epsilon}^a)\{C + D(\frac{\dot{\epsilon}}{\dot{\epsilon}_0})^b\}(1 - T^{*c}) \quad (15)$$

Table 2 Constants for the modified JC model

<i>A/MPa</i>	<i>B/MPa</i>	<i>C</i>	<i>D</i>	<i>a</i>	<i>b</i>	<i>c</i>	<i>d/ J</i>
311.22	240.11	0.46	0.49	0.28	0.10	0.68	1.2e-4

Table 3 Comparison of classical and modified JC models

	Classical JC model	Modified JC model
Strain hardening	Characterized based on quasi-static test	Characterized based on quasi-static test
Strain rate hardening	Inaccurate prediction beyond strain rate of $10^3 /s$	Accurate prediction up to strain rate $10^5 /s$
Thermal softening	Characterized based on tests at elevated temperatures	Characterized based on tests at elevated temperature
Acoustic softening	Not available	Characterized based on acoustic softening studies

Implementation of Material Model

The modified JC model is implemented in the finite element commercial software ABAQUS 6.14 using the user-defined material subroutine. The material model is integrated for computing the global stiffness matrix. Given the load increment, the stiffness matrix is then used for finding the displacement and strain increments that enable the system to reach quasi-static equilibrium. If equilibrium cannot be reached, the load increment will be reduced and the procedure is repeated. The steps are shown as follows. In the global level, the dynamics of the system is written as [28]:

$$\mathbf{M}\ddot{\mathbf{u}} + \mathbf{C}\dot{\mathbf{u}} + \mathbf{K}\mathbf{u} = \mathbf{f} \quad (16)$$

\mathbf{M} is the global mass matrix, \mathbf{C} is the global damping matrix, \mathbf{K} is the global stiffness matrix, and \mathbf{f} is external force vector. The dynamic equation is solved explicitly by decomposing each time step into a large number of small time increments. At each time increment, the quasi-static equilibrium is reached at each material point. The equation is written as:

$$\mathbf{K}\mathbf{u} = \mathbf{f} \quad (17)$$

\mathbf{K} can be further decomposed:

$$\mathbf{K} = \int \mathbf{B}^T \mathbf{D}^{ep} \mathbf{B} d\Omega \quad (18)$$

\mathbf{B} is the deformation matrix, \mathbf{D}^{ep} is the elastic-plastic constitutive matrix that is defined by the material model. Write equation (17) into incremental form:

$$\mathbf{K}\Delta\mathbf{u} = \Delta\mathbf{f} \quad (19)$$

Since

$$\Delta\mathbf{u} = \mathbf{B}^{-1}\Delta\boldsymbol{\varepsilon} \quad (20)$$

Where $\Delta\boldsymbol{\varepsilon}$ is the incremental strain. Inserting equations (18) and (20) into equation (19) yields:

$$\mathbf{B}^T \mathbf{D}^{ep} \Delta\boldsymbol{\varepsilon} = \Delta\mathbf{f} \quad (21)$$

Since \mathbf{D}^{ep} depends implicitly on $\Delta\boldsymbol{\varepsilon}$, $\Delta\boldsymbol{\varepsilon}$ is found by integrating the constitutive law defined by the material model. Two integration schemes are available: explicit or implicit. In this work, both integration schemes have been explored and the explicit integration is implemented. The selection process is explained in the following section. When \mathbf{D}^{ep} is determined, the stress increment can be obtained accordingly using the following equation.

$$\Delta\sigma = \mathbf{D}^{ep}\Delta\epsilon \quad (22)$$

Inserting equation (22) to (21) yields the incremental relation between $\Delta\sigma$ and $\Delta\mathbf{f}$ which leads to a differential relation. This relation can be integrated over the material domain and yields:

$$\int \mathbf{B}^T \sigma d\Omega = \int \mathbf{f} d\Omega \quad (23)$$

Let $\mathbf{q} = \int \mathbf{B}^T \sigma d\Omega$, then a force residual \mathbf{r} is defined:

$$\mathbf{r} = \mathbf{q} - \mathbf{f} \quad (24)$$

The force residual is used a convergence criterion for numerical integration and is checked at each iteration to see if equilibrium is achieved.

To sum up, the general algorithm is as follow:

1. Apply a load increment $\Delta\mathbf{f}$, calculate for displacement increment $\Delta\mathbf{u}$ and strain increment $\Delta\epsilon$.
2. Compute the stress increment $\Delta\sigma$
3. Compute the residual \mathbf{r}
4. If the residual \mathbf{r} exceeds a set tolerance, set $\Delta\mathbf{f} = -\mathbf{r}$ and return to step 1.

In step 1, $\Delta\epsilon$ can be obtained either through explicit or implicit scheme. The two integration schemes are explained briefly. For the explicit integration scheme, the strain difference is decomposed into elastic and plastic contributions:

$$d\epsilon = d\epsilon_e + d\epsilon_p \quad (25)$$

The relation between elastic stress and strain can thus be written:

$$d\sigma = \mathbf{D}(d\epsilon - d\epsilon_p) \quad (26)$$

Where \mathbf{D} is the elastic stiffness matrix. First introduce the von Mises yield function for isotropic hardening:

$$f(\sigma, \epsilon_p) = f(\sigma) - r(\epsilon_p) - \sigma_y = \mathbf{0} \quad (27)$$

Where r is the isotropic hardening term, and σ_y is the initial yield stress. Then introduce the consistency condition:

$$df(\sigma, \epsilon_p) = \frac{\partial f(\sigma)}{\partial \sigma} d\sigma - \frac{\partial r}{\partial \epsilon_p} d\epsilon_p = \mathbf{0} \quad (28)$$

And third the associated flow rule:

$$d\boldsymbol{\varepsilon}_p = d\lambda \frac{\partial f(\boldsymbol{\sigma})}{\partial \boldsymbol{\sigma}} \quad (29)$$

Where $d\lambda$ is a multiplier that represents the magnitude of the plastic strain difference and $\frac{\partial f(\boldsymbol{\sigma})}{\partial \boldsymbol{\sigma}}$ represents the flow direction of the plastic strain difference. By performing some algebraic operations on equation (27)-(29), the magnitude of the plastic strain difference $d\lambda$ can be derived in explicit form:

$$d\lambda = \frac{\mathbf{n} \mathbf{D}}{\mathbf{n} \cdot \mathbf{D} \mathbf{n} + H} d\boldsymbol{\varepsilon}_e \quad (30)$$

Where $\mathbf{n} = \frac{\partial f(\boldsymbol{\sigma})}{\partial \boldsymbol{\sigma}}$ is the normal direction of the plastic flow. $H = \frac{dr}{d\varepsilon_p}$, r is the isotropic hardening term. \mathbf{D} is the elastic stiffness matrix. f is the yield function. $d\lambda$ is the magnitude of $d\boldsymbol{\varepsilon}_p$. Apply forward Euler explicit integration scheme, equation (30) can be written in von Mises plasticity as:

$$d\lambda = \frac{\bar{\sigma} - \sigma_y}{3G + H} d\varepsilon_e \quad (31)$$

Where $\bar{\sigma}$ is the von Mises stress defined as $\bar{\sigma} = \sqrt{\frac{3}{2} \boldsymbol{\sigma} : \boldsymbol{\sigma}}$ and σ_y is the yield stress. The explicit scheme is relatively simple to implement and does not require the update of Jacobian matrix. However, it is conditionally stable and requires the time increment to be smaller than a critical threshold defined as:

$$\Delta t_{cr} \approx \frac{L_c}{c_d} \quad (32)$$

Where L_c is the characteristic length of the element and c_d is the dilatational wave speed.

The implicit integration scheme decomposes $d\boldsymbol{\varepsilon}$ into an elastic trial strain $d\boldsymbol{\varepsilon}_e^{tr}$ and a plastic corrective strain $d\boldsymbol{\varepsilon}_p^c$:

$$d\boldsymbol{\varepsilon} = d\boldsymbol{\varepsilon}_e^{tr} - d\boldsymbol{\varepsilon}_p^c \quad (33)$$

Write the Hooke's law in tensorial form and introduce the flow rule (equation (28)) and equation (33), with some algebra:

$$\bar{\sigma} + 3G\Delta\lambda = \bar{\sigma}^{tr} \quad (34)$$

Where $\bar{\sigma}$ is the von Mises stress and $\bar{\sigma}^{tr}$ is defined as $\bar{\sigma}^{tr} = \sqrt{\frac{3}{2}\boldsymbol{\sigma}^{tr}:\boldsymbol{\sigma}^{tr}}$. Insert equation (34) into the yield function (equation (27)):

$$\bar{\sigma}^{tr} - 3G\Delta\lambda - r - \sigma_y = 0 \quad (35)$$

Since r is a function of $\Delta\lambda$, the equation is solved implicitly using Newton's method. The infinitesimal difference of the corrective plastic strain increment is derived:

$$d\Delta\lambda = \frac{3G(\bar{\varepsilon}^{tr} - \Delta\lambda) - r - \sigma_y}{3G + H} \quad (36)$$

Where $\bar{\varepsilon}^{tr}$ is the von Mises strain defined as $\bar{\varepsilon}^{tr} = \sqrt{\frac{2}{3}\boldsymbol{\varepsilon}^{tr}:\boldsymbol{\varepsilon}^{tr}}$. With $d\Delta\lambda$ the being computed, the stress and strain increments can be updated. The Jacobian matrix is then updated accordingly using the following equation:

$$\mathbf{J} = \frac{\partial\Delta\boldsymbol{\sigma}}{\partial\Delta\boldsymbol{\varepsilon}} \quad (37)$$

The implicit scheme is unconditionally stable since the yield criterion is imposed at each iteration. Therefore the time increment is not necessarily small and the increment length can be adjusted as iteration proceeds for optimum computational efficiency. However, the implicit iteration for computing $\Delta\lambda$ and the update of Jacobian matrix \mathbf{J} are computationally costly.

By implementing both the implicit and explicit integration scheme for solving the material model, it is found that the explicit scheme requires much less time than the implicit scheme for computing the stress-strain relation of a quasi-static tensile test. Moreover, the implicit scheme suffers from convergence difficulties as material and geometric nonlinearity increases. The implicit scheme is more sensitive to mesh resolution, loading speed, and nonlinearity of the material model than the explicit scheme. As a result, the explicit scheme is selected for integrating the modified JC material model. A user-defined material subroutine (VUMAT) is developed for implementation of the model in ABAQUS. The work flowchart of the VUMAT is shown in fig.8.

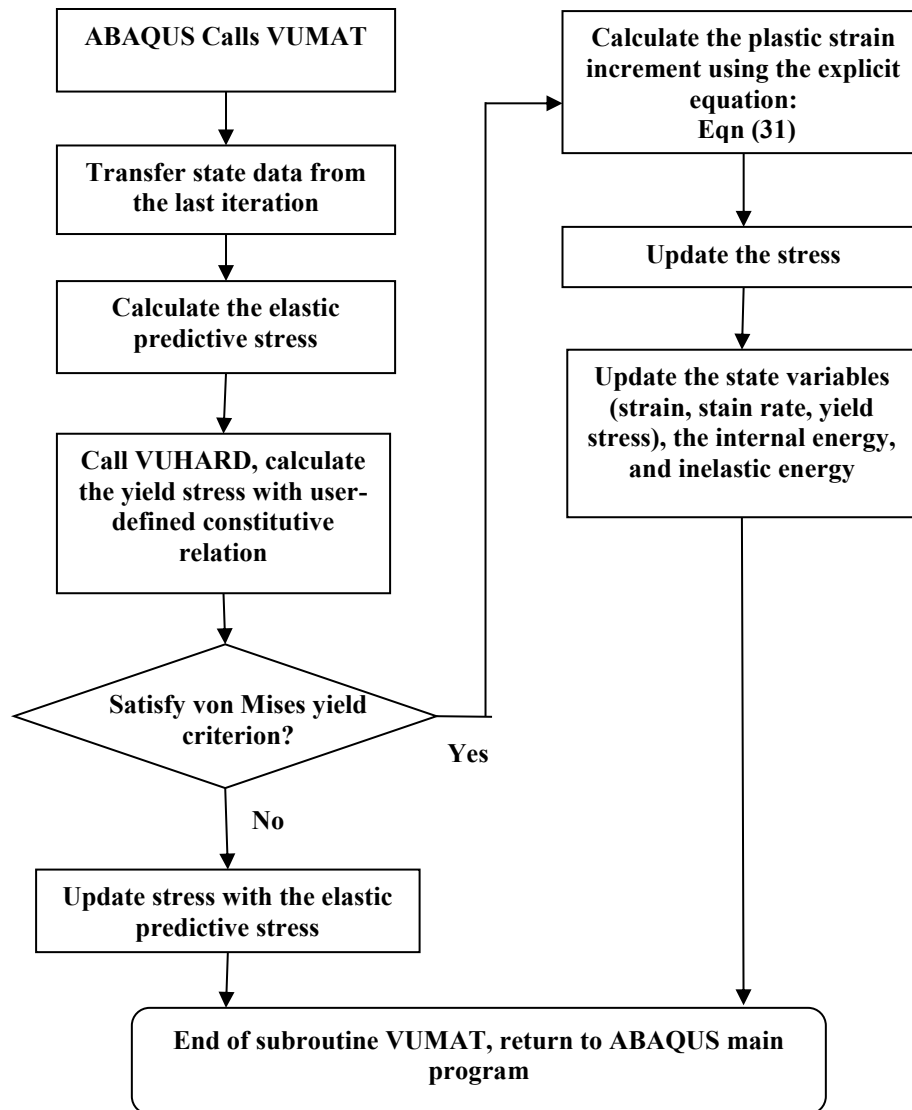


Fig.8 flowchart of VUMAT

Validation of Material Model

The modified JC model is first implemented in simple finite element models for validation. Specifically, three validations have been carried out: 1) 1-D tensile test subjected to ultrasonic vibrations with different amplitudes 2) 1-D tensile tests at high strain rates and 3) 3-D quasi-static tensile test. The predicted flow stress-plastic strain curves from the first two tests are compared with those from the analytical models (fig. 8). In the tensile test under ultrasonic vibration (fig. 8 (a)), the simulated curves run parallel to the analytical curves with slight deviation possibly due to error introduced by the explicit integration scheme. The maximum relative error for the prediction is 2.9%. In the strain rate test (fig. 8 (b)), the simulated stress-strain curves demonstrates serrated shapes at elevated strain rates possibly due to effects of dynamic loading as well as the elastic predictor-plastic corrector algorithm implemented in VUMAT. Despite the serrated shape, the simulated curves run parallel to the analytical curves and the relative errors are small. The errors

are larger at elevated strain rates and the maximum value is 6.4%. Fig. 9 (a) shows the comparison between stress-strain curves from the 3-D quasi-static tensile simulation and from the experiment. The 3-D model is built such that the dimensions are the same as the standard tensile test specimen used in experimental studies (fig. 9 (b)). Only one quarter of the model is built for computational efficiency. The prediction from the finite element aligns well with the experimental stress-strain curve in both elastic and plastic deformation regions.

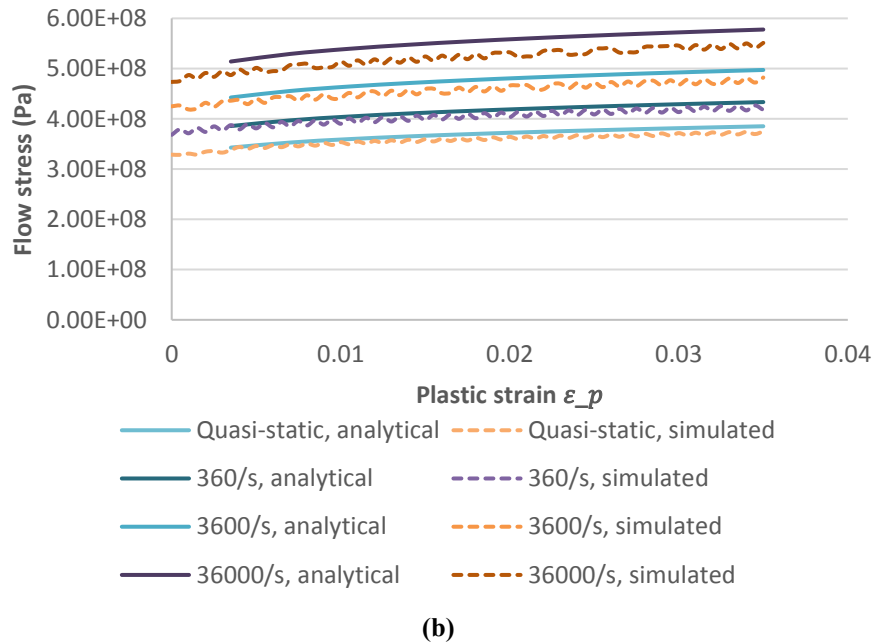
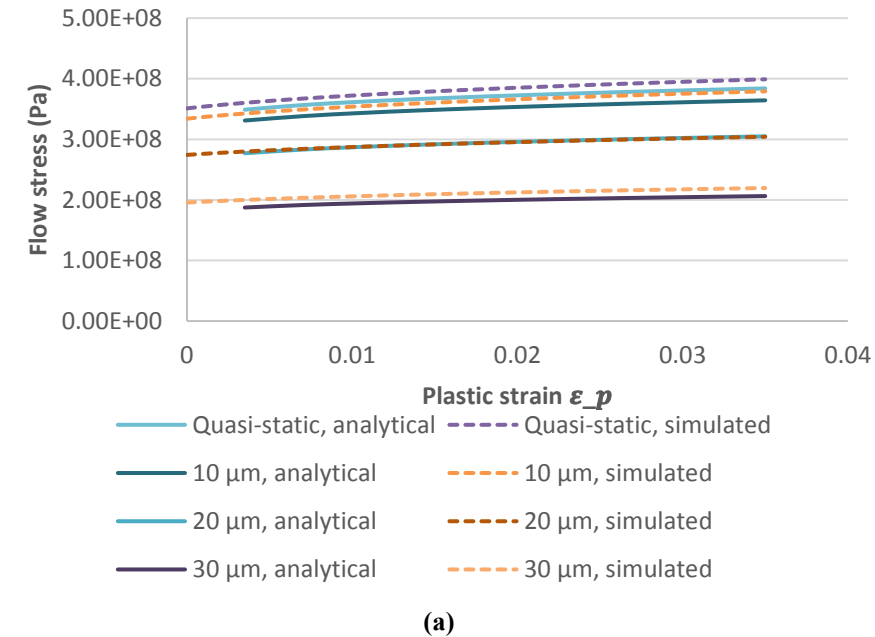


Fig. 8 (a) Stress-strain curves with different vibration amplitudes: 10, 20, and 30 μm . (b) Stress-strain curves with different strain rates: 360/s, 3600/s, and 36000/s.

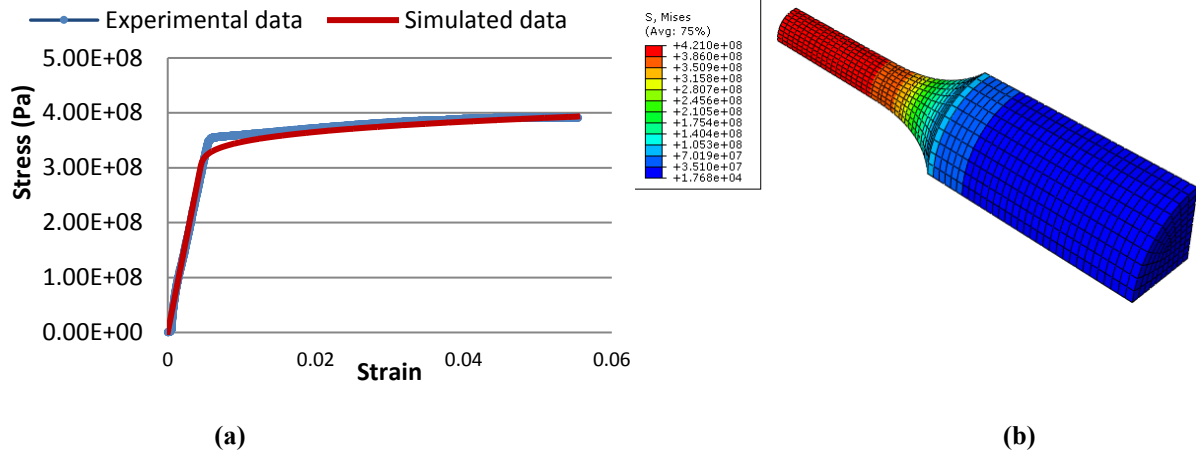


Fig. 9 (a) The experimental and simulated stress strain curves generated from quasi-static tensile tests on aluminum 6061-T6. (b) The 3-D finite element model of one quarter of the standard tensile specimen

The UAM Model

In order to understand how the changing dynamics of the system affect the bonding mechanics, a 3-D UAM model is built using ABAQUS. The model introduces a sonotrode, a top foil, and a built feature (fig. 10 (a)). Several simplifications are made in building the model. The sonotrode is modeled using rigid shell elements whereas the top foil and built features are modeled as deformable solid since the Titanium sonotrode is much harder than the foils. The laminar built feature is simplified as a parallelepiped assuming that no interfacial sliding takes place between two bonded layers. It should be noted that during welding severe plastic deformation is observed only in a region close to the weld interface. The region is characterized by the refinement and “flow” like morphology of the sub-grains and is typically 10 – 60 μm in depth from the weld interface [29]. As a result, two plastic deformation layers are introduced and attached to the mating surfaces of the top foil and the built feature respectively (fig.10 (b)). The elasticity and plasticity of the material in the plastic deformation layers differ from those of the bulk material of the top foil and the built feature. Specifically, acoustic softening only takes place in the layer and therefore the yield stresses are much lower in the layer than in the bulk material. The effective elastic modulus is also reduced by the surface asperities which have much lower stiffness than the bulk material. When under compression loading, the surface asperities are much easier to undergo plastic deformation than the bulk materials underneath. The effective modulus can be determined by assuming a Hertzian contact between two rough surfaces [30]:

$$\frac{1}{E^*} = \frac{1-\nu_1^2}{E_1} + \frac{1-\nu_2^2}{E_2} \quad (38)$$

Where E_1 , E_2 , ν_1 , ν_2 are the elastic modulus and Poisson’s ratio of the two materials in contact. For the contact between aluminum 6061-T6 foils, the effective modulus is roughly half of the elastic modulus: $E^* = 0.56E$. The lowered elastic modulus and yield stress allow for severe plastic deformation to take place at the weld interface. Both plastic layers are 20 μm thick according to observation made by Johnson et al. and the overall thickness of the top foil is 150 μm [29].

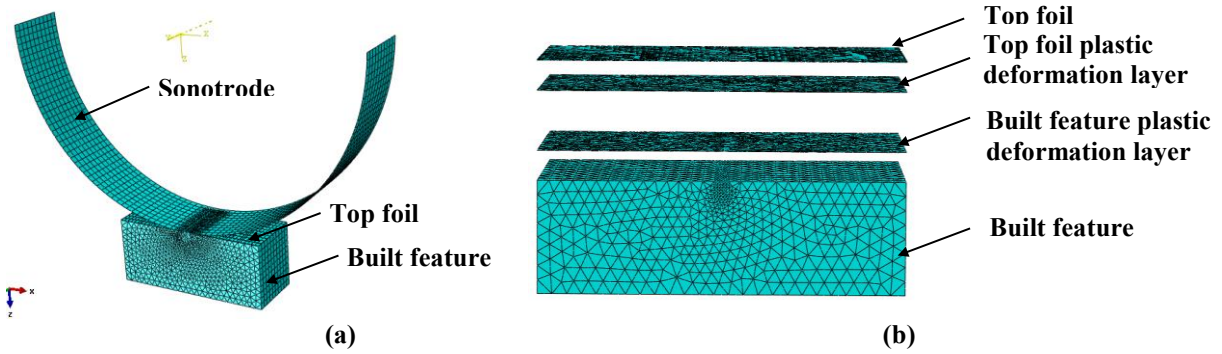


Fig. 10 (a) UAM model overview (b) The plastic deformation layers between the top foil and built feature (the sonotrode is removed for clarity)

Boundary conditions imposed on the sonotrode include a compression load of 1600 N in normal direction and a sinusoidal displacement of 20 μm at 20 kHz along the width of the foil horizontal direction. Clamping is imposed at the bottom of the built feature. As the sonotrode rolls along the length of the built feature, the part of top foil behind the rolling path is already “bonded” and thus are fully constrained to the built feature.

Contact interactions are defined between sonotrode and top foil as well as between the top foil and the built feature. In the direction normal to contact interface, a surface-to-surface “hard” contact is defined which minimizes the penetration of the slave surface (soft material) into the master surface (hard material) at the contact locations using penalty method and impedes the transfer of tensile stress across the interface [28]. In tangential direction, a stick/slip criterion is imposed followed by a critical shear stress τ_{cr} being defined such that the surfaces in contact stick as $\tau < \tau_{cr}$, and slip as $\tau > \tau_{cr}$. The value of τ_{cr} is calculated based on isotropic Coulomb’s law: the product of friction coefficient and normal pressure. The friction coefficient between the top foil and substrate is set to 0.4 based on previous experimental studies [12], whereas at the sonotrode-foil interface a “rough” surface contact is defined which imposes no slip at the interface. The assumptions of friction coefficient being a constant and the top being “grabbed” by the sonotrode without slipping are ideal assumptions for simplifying the problem. The influences of these factors will be covered in future work.

In order to capture the severe deformation underneath the sonotrode with sufficient accuracy and at the same time reduce computational cost, a contact patch is generated with refined mesh for the top foil, built feature, and plastic deformation layers in between. The 4-node linear tetrahedral element (C3D4) is selected due to its robustness over hexagonal shape and being able to adapt to relatively complex geometries. The linear elements is preferred over quadrature due to its robustness under contact conditions which leads to less convergence issues. The mesh size is determined based on the criterion of being able to predict modal frequencies with sufficient accuracy and capture the Hertzian contact stress distribution [33].

The ABAQUS Explicit solver is used to interface with the user defined subroutine VUMAT for solving the model. The simulation is run on a high-performance computing (HPC) cluster with 16 processors for roughly 8 hours (Intel Xeon processors, 2.33 GHz). The simulation time is set to 0.3 ms which covers 6 vibration cycles of the sonotrode. Since the rolling speed (0.03 m/s) is much lower than the vibration speed (0.4-4 m/s), the sonotrode is assumed to be dwelling and only

ultrasonic vibration is considered in the simulation. Table 4 shows the operating parameters used for simulating the UAM process. The height of the built feature is varied such that the height-to-width ratio (H/W) is set to 0.2, 0.8, 1, 0.5, and 2 while the width and the length are fixed. As the height-to-width ratio varies, the dynamic interaction between the sonotrode and the built feature changes accordingly. Fig. 11 shows the sonotrode amplitude (dash line) dynamic response (colored solid lines) of the built feature at various H/W. It is obvious that as the height-to-width ratio reaches 1, the response amplitude reaches the maximum in phase with the sonotrode, leading to insufficient differential motion between the built feature and the sonotrode for sustaining interfacial friction and forming bonds. At the height-to-width ratio of 0.2 and 1.5, the responses amplitudes are the minimum which is in agreement with the conclusion made by Gibert et al. that bonding can be reinitiated once the critical height-to-width ratio is exceeded [31]. At height-to-width ratio of 2, the response amplitude increases slightly possibly due to the loss of static stiffness as height increases.

Table 4. The operating parameters used for UAM simulation

Vibration amplitude	Vibration frequency	Compression load	Weld speed	Temperature
10 μm	20 kHz	1600 N	0 m/s	150 $^{\circ}\text{C}$

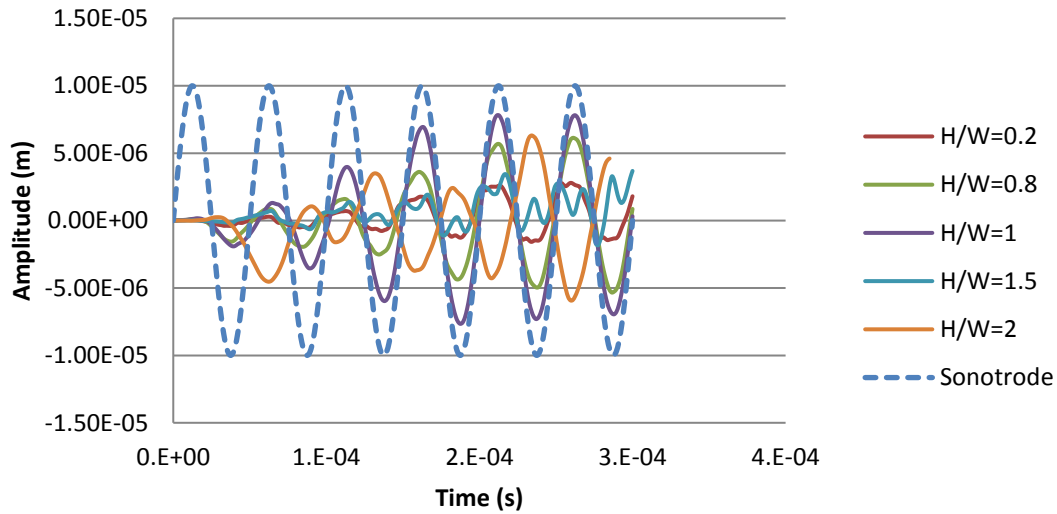


Fig. 11 (a) UAM model overview (b) The plastic deformation layers between the top foil and built feature (the sonotrode is removed for clarity)

The plastic deformation of both top foil and built feature are measured in the weld region in terms of von Mises stress. The measurement are taken from the plastic deformation layers of both the top foil and the built feature. The measuring points are located within the contact patch underneath the sonotrode (fig. 12). Fig. 13 shows the von Mises stress history of four different measuring locations at different height-to-width ratios. Several interesting observations can be made. First, at height-to-width ratio of 0.2, the von Mises stresses at all four measuring points exceed the yield stress which is indicated by the dash line. The actual yield stress (300 MPa) is lower than the nominal yield stress (350 MPa) under the effect of ultrasound and elevated temperature. At aspect ratio of 1.0, however, only one measuring point (edge of the top foil)

undergoes plastic deformation whereas three other points are all deformed elastically, which indicates insufficient plastic deformation at both measuring points. The results agrees well with the experimental observations made by Robinson et al [18]. Second, by comparing the von Mises stresses at the edge and the center, it is shown that the stresses at the edge are generally higher than at the center in both top foil and the built feature. This could be due to the variation in differential motion across the width of the contact patch. The differential motion at the center are generally smaller than that in the edge thus causing the von Mises stress to be lower. This observation further points to the possible change of locations of bond degradation due to the change of height-to-width ratio.

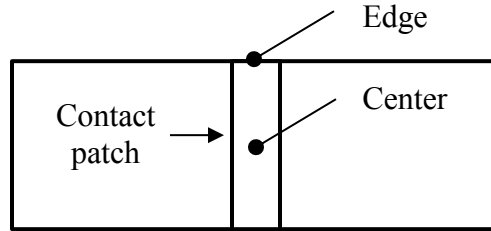


Fig. 12 The location of measuring points in the top view of top foil/built feature

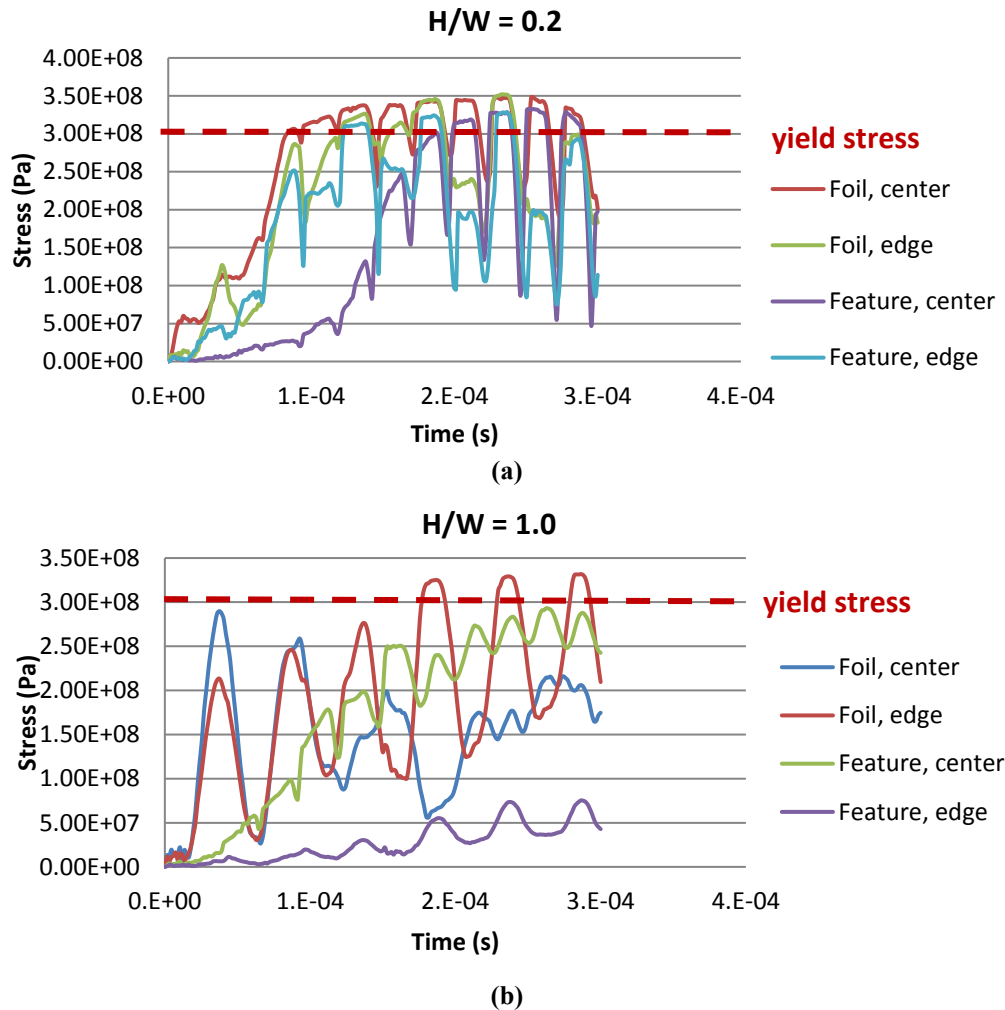


Fig. 13. (a) The von Mises stress history at $H/W = 0.2$. (b) The von Mises stress history at $H/W = 1.0$

Conclusion and Future Work

In this work, an elastic-plastic material model is developed and evaluated specifically for the UAM process. The model is derived by overcoming some of the limitations of the Johnson-Cook model when implemented for UAM. The material model is then implemented in a finite element UAM model for predicting material deformation at the bond interface under the influence of the dynamics and stick-slip friction of the system. The change of macroscopic dynamics of the built feature is shown to have a significant influence on the plastic deformation at the local bond interface. Specifically, the model first shows the significant change of dynamic response of the built feature at different aspect ratios. Then by comparing the evolution of von Mises stresses at different aspect ratios, the plastic deformation is shown to be significantly reduced at all measuring points at the critical aspect ratio ($H/W = 1$). The stress evolution also shows a variation of plastic deformation across the width of the built feature. The material undergoes slightly more plastic deformation at the edge than at the center. These preliminary results have shown that the UAM model is capable of predicting material deformation at the bonding interface by considering a variety of influential factors: the dynamics of the system, strain and strain rate hardening, the acoustic and thermal softening, and stick-slip friction. The plastic deformation serves as an effective indicator of the bond quality and allows for the model to be able to quantify the bond quality based on the UAM operating parameters (amplitude, compression, weld speed).

Following these preliminary results, the UAM model needs to be improved in several aspects: 1) a thermo-mechanical model is to be built to replace the current model in which the bonding process is assumed isothermal. 2) A temperature-dependent friction model needs to be established for more accurate prediction of thermal effects. 3) A set of criteria needs to be established to quantify the bond quality based on the prediction from the UAM model.

Acknowledgement

This research was partially supported by the National Science Foundation under grant # 1068977 entitled “Understanding the Macroscopic Dynamics of Ultrasonic Consolidation”. The views presented in this work do not necessarily reflect those of our sponsor whose support is gratefully acknowledged. We also wish to thank Ms. Sophie Morneau from Branson Ultrasonics Corporation for loaning some ultrasonic components.

Reference

- [1] White, D. (2003). Ultrasonic consolidation of aluminum tooling. *Advanced Materials & Processes*.
- [2] Kong, C. Y., Soar, R. C., & Dickens, P. M. (2003). Characterisation of aluminium alloy 6061 for the ultrasonic consolidation process. *Materials Science and Engineering: A*, 363(1-2), 99–106. doi:10.1016/S0921-5093(03)00590-2
- [3] Ram, G. D. J., Yang, Y., Nylander, C., Aydelotte, B., Stucker, B. E., & Adams, B. L. (2007). Interface Microstructures and Bond Formation in Ultrasonic Consolidation, 266–283.

- [4] Lee, S. S., Kim, T. H., Hu, S. J., Cai, W. W., Abell, J. A., & Li, J. (2013). Characterization of joint quality in ultrasonic welding of battery tabs. *Journal of Manufacturing Science and Engineering*, 135(2), 21004.
- [5] De Vries, E. (2004). Mechanics and mechanisms of ultrasonic metal welding
- [6] Gunduz, I. E., Ando, T., Shattuck, E., Wong, P. Y., & Doumanidis, C. C. (2005). Enhanced diffusion and phase transformations during ultrasonic welding of zinc and aluminum. *Scripta Materialia*, 52(9), 939–943. doi:10.1016/j.scriptamat.2004.12.015
- [7] Joshi, K. (1971). The formation of ultrasonic bonds between metals. *Welding Journal*.
- [8] Keller, D. V.; Tsai, M. Adhesion. (1968) Between Automatically Pure Metallic Surfaces, Technical Report.
- [9] De Vries, E. (2004). *Mechanics and mechanisms of ultrasonic metal welding*.
- [10] Kenik, E., & Jahn, R. (2003). Microstructure of ultrasonic welded aluminum by orientation imaging microscopy. *Microscopy and Microanalysis*, 9(S02), 720–721.
- [11] Gibert, J. M., Fadel, G., & Daqaq, M. F. (2013). On the stick-slip dynamics in ultrasonic additive manufacturing. *Journal of Sound and Vibration*, 332(19), 4680-4695.
- [12] Zhang, C., & Li, L. (2007). Effect of friction on ultrasonic consolidation. *ASME 2007 International*
- [13] Siddiq, A., & Ghassemieh, E. (2008a). Thermomechanical analyses of ultrasonic welding process using thermal and acoustic softening effects. *Mechanics of Materials*, 40(12), 982–1000.
- [14] Kelly, G., & Advani, S. (2013). A model to characterize acoustic softening during ultrasonic consolidation. *Journal of Materials*
- [15] Siddiq, A., & El Sayed, T. (2011). Acoustic softening in metals during ultrasonic assisted deformation via CP-FEM. *Materials Letters*, 65(2), 356–359. doi:10.1016/j.matlet.2010.10.031
- [16] Lemaitre, J., & Chaboche, J. L. (1994). *Mechanics of solid materials* (p. 584). Cambridge university press.
- [17] Langenecker, B. (1966). Effects of ultrasound on deformation characteristics of metals. *Sonics and Ultrasonics, IEEE Transactions on*.
- [18] Robinson, C., Zhang, C., & Ram, G. (2006). Maximum height to width ratio of freestanding structures built using ultrasonic consolidation. *Proceedings of 17th ...*, 502–516.
- [19] Johnson, G. R., & Cook, W. H. (1983, April). A constitutive model and data for metals subjected to large strains, high strain rates and high temperatures. In *Proceedings of the 7th International Symposium on Ballistics* (Vol. 21, pp. 541-547).
- [20] Lesuer, D. R., Kay, G., & LeBlanc, M. (1999). Modeling large strain, high rate deformation in metals. *Engineering research, development and technology*.
- [21] Sakino, K. (2006, August). Strain rate dependence of dynamic flow stress considering viscous drag for 6061 aluminium alloy at high strain rates. In *Journal de Physique IV (Proceedings)* (Vol. 134, pp. 183-189). EDP sciences.
- [22] Nicholas, T. (1981). Tensile testing of materials at high rates of strain. *Experimental Mechanics*, 21(5), 177-185.
- [23] Frost, H. J., & Ashby, M. F. (1982). Deformation mechanism maps: the plasticity and creep of metals and ceramics.
- [24] Manes, A., Peroni, L., Scapin, M., & Giglio, M. (2011). Analysis of strain rate behavior of an Al 6061 T6 alloy. *Procedia Engineering*, 10, 3477-3482.
- [25] Yadav, S., Chichili, D. R., & Ramesh, K. T. (1995). The mechanical response of a 6061-T6 Al/Al₂O₃ metal matrix composite at high rates of deformation. *Acta Metallurgica et Materialia*, 43(12), 4453-4464.

- [26] Mao, Q., Coutris, N., & Fadel, G. (2014). Characterization of acoustic softening of aluminum 6061 within a plasticity framework. International Solid Freeform Fabrication Symposium-an Additive Manufacturing Conference, Austin, Texas.
- [27] Frederick, J. R. (1965). Ultrasonic engineering.
- [28] Manual, Abaqus Users. "Version 6.14-1." *Dassault Systèmes Simulia Corp., Providence, RI.*
- [29] Johnson, K., Edmonds, H. C., Higginson, R. L., & Harris, R. A. (2011). New discoveries in ultrasonic consolidation nano-structures using emerging analysis techniques. Proceedings of the Institution of Mechanical Engineers, Part L: Journal of Materials Design and Applications, 0954420711413656.
- [30] Johnson, K. L. (1974). Contact mechanics, 1985.
- [31] Gibert, J. M., McCullough, D. T., Fadel, G. M., Martin, G. K., & Austin, E. M. (2009, January). Stick-slip dynamics in ultrasonic consolidation. In ASME 2009 International Design Engineering Technical Conferences and Computers and Information in Engineering Conference (pp. 307-317). American Society of Mechanical Engineers.
- [32] Kelly, G. S., Just, M. S., Advani, S. G., & Gillespie, J. W. (2014). Energy and bond strength development during ultrasonic consolidation. *Journal of Materials Processing Technology*, 214(8), 1665-1672.
- [33] Yang, Y., Janaki Ram, G. D., & Stucker, B. E. (2010). An analytical energy model for metal foil deposition in ultrasonic consolidation. *Rapid Prototyping Journal*, 16(1), 20-28.